Mixing Measurements on an Equatorial Ocean Mooring

J. N. MOUM AND J. D. NASH

College of Oceanic and Atmospheric Sciences, Oregon State University, Corvallis, Oregon

(Manuscript received 20 December 2007, in final form 9 April 2008)

ABSTRACT

Vaned, internally recording instruments that measure temperature fluctuations using FP07 thermistors, including fluctuations in the turbulence wavenumber band, have been built, tested, and deployed on a Tropical Atmosphere Ocean (TAO) mooring at 0°, 140°W. These were supplemented with motion packages that measure linear accelerations, from which an assessment of cable displacement and speed was made. Motions due to vortex-induced vibrations caused by interaction of the mean flow with the cable are small (rms < 0.15 cable diameters) and unlikely to affect estimates of the temperature variance dissipation rate χ_T. Surface wave–induced cable motions are significant, commonly resulting in vertical displacements of ± 1 m and vertical speeds of ± 0.5 m s^{-1} on 2–10-s periods. These motions produce an enhancement to the measurement of temperature gradient in the surface wave band herein that is equal to the product of the vertical cable speed and the vertical temperature gradient (i.e., $dT/dt \sim w_c dT/dz$). However, the temperature gradient spectrum is largely unaltered at higher and lower frequencies; in particular, there exists a clear scale separation between frequencies contaminated by surface waves and the turbulence subrange. The effect of cable motions on spectral estimates of χ_T is evaluated and determined to result in acceptably small uncertainties ($<$ a factor of two 95% of the time, based on 60-s averages). Time series of χ_T and the inferred turbulent kinetic energy dissipation rate ϵ are consistent with historical data from the same equatorial location.

1. Motivation

The need for extended observations of mixing is highlighted by the potentially prominent role played by mixing in changing equatorial SST on interannual (El Niño) time scales. Coincident with the passage of a downwelling Kelvin wave observed prior to the 1991–93 El Niño, reduced mixing observed by Lien et al. (1995) may have provided positive feedback toward increasing SST in the central Pacific. At the other extreme, enhanced subsurface mixing is a prime (but unproven) candidate for the 8°C surface cooling (in 1 month) at 0 125°W to abruptly conclude the strong 1997–98 El Niño (McPhaden 1999; Wang and McPhaden 2001). This enhanced mixing, inferred from bulk estimates, must also be highly intermittent (characteristic of naturally occurring turbulence) and not amenable to observation from shipboard campaigns, which are infrequent, of necessarily short duration, and must be planned years in advance. This is exemplified by three experiments to examine the nature of turbulent mixing in the central equatorial Pacific: in 1984, TROPIC HEAT (Moum and Caldwell 1989); in 1987, TROPIC HEAT 2 (Moum et al. 1992a); and in 1991, the Tropical Instability Wave Experiment (TIWE; Lien et al. 1995). All of these experiments focused on the site at 0°, 140°W, largely because of the presence of long-term moored observations predating the full implementation of the Tropical Ocean and Global Atmosphere–Tropical Atmosphere Ocean (TOGA–TAO) equatorial array of moorings (McPhaden 1993). The sum duration of these intensive profiling observations was about 100 days over a period of 7 yr, with none since 1991. Moreover, mixing parameterizations based on these experiments have not been particularly successful (Zaron and Moum 2008, manuscript submitted to *J. Phys. Oceanogr.*). Reliably establishing the role of mixing in interannual climate phenomena such as El Niño is impossible without longer-term records.

To progress toward the goal of establishing extended observations of mixing and internal gravity waves, we have developed, tested, and deployed a string of moored temperature microstructure recorders (χpods; Fig. 1) at the 0°, 140°W TAO mooring site. The initial

Corresponding author address: J. N. Moum, College of Oceanic and Atmospheric Sciences, Oregon State University, COAS Admin. Bldg. 104, Corvallis, OR 97331–5503.
E-mail: moum@coas.oregonstate.edu

DOI: 10.1175/2008JTECHO617.1

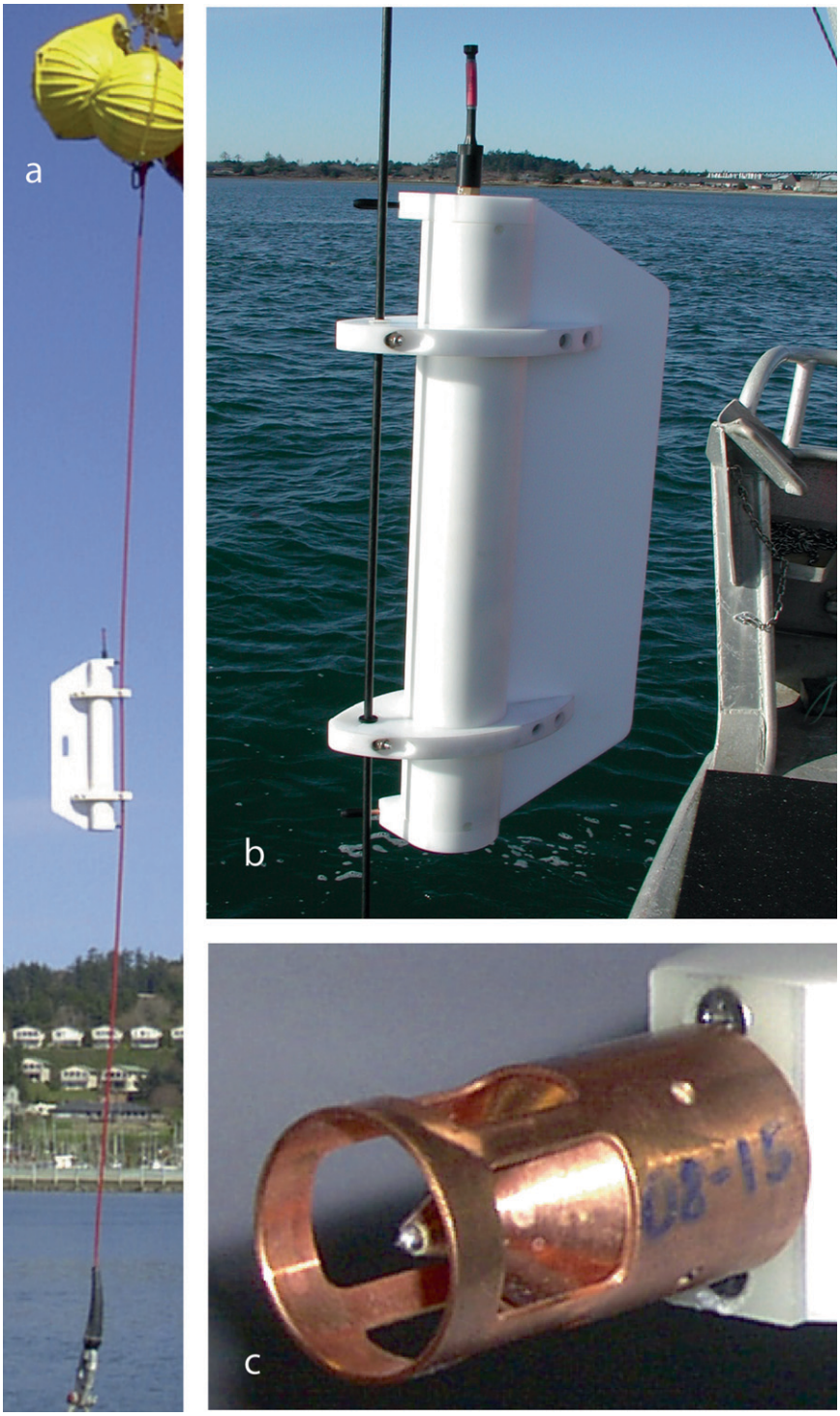

FIG. 1. (a) χpod attached to cable over the dock in Yaquina Bay for testing, (b) a closer look at the cable attachment, and (c) close-up of thermistor sting with protector. The diameter of the protective ring is 18 mm. The thermistor bead is set back 4 mm from the leading edge of the ring.

deployment yielded a highly resolved, 4-month time series of temperature T, the rate of dissipation of temperature gradient fluctuations χ_T, the turbulent kinetic energy dissipation rate ϵ, and the turbulence diffusion coefficient K_T at three depths over the range 30–90 m. We have since attempted to maintain a presence at 0°, 140°W and have deployed χpods at three to six depths continually since September 2005.

Our objective is to provide a simple, reliable, and affordable device that can be readily integrated into existing moorings or autonomous vehicles. We expect these measurements will provide a meaningful beginning toward the objectives of dynamically linking the mixing to the larger spatial scales and longer time scales at this and other locations.

In this paper, we describe the basic configuration and philosophy behind χpod, some of the lessons we have learned from our first deployment, and some preliminary results. We begin with a set of definitions and our procedure for estimating χ_T (section 2), followed by a summary of design considerations (section 3). The configuration of χpod is discussed in section 4. We then present some basic results, including measurements of the cable motion (section 5). The effect of cable motion is critical to our estimate of χ_T and is discussed in section 6. This is followed by a comparison to historical data (section 7) and, finally, a summary and conclusions (section 8).

2. Definitions and procedures

a. χ_T, ϵ, and K_T

The ultimate objective of these mixing measurements is the computation of χ_T, ϵ, K_T, the turbulent heat and buoyancy fluxes $K_T dT/dz$ and $N^2 K_T$, and their vertical divergences. Here, $N^2 = -g/\rho \cdot d\rho/dz$ is the squared buoyancy frequency, g is the acceleration due to gravity, and ρ is density.

With fully resolved measurements of ∇T in the diffusive subrange of turbulence, the dissipation rate of temperature variance can be computed as

$$\chi_T = 2D_T \left\langle \frac{dT}{dx_i} \frac{dT}{dx_i} \right\rangle, \tag{1}$$

which for isotropic turbulence becomes

$$\chi_T = 6D_T \left\langle \frac{dT}{dx} \frac{dT}{dx} \right\rangle = 6D_T \int_0^\infty \Psi_{T_x}(k)\, dk, \tag{2}$$

where dT/dx is the alongpath (not necessarily horizontal at all wavenumbers) component of temperature gradient, D_T the thermal diffusivity, and $\Psi_{T_x}(k)$ the wavenumber spectrum of dT/dx. The brackets ideally refer to an ensemble average; in this particular case, they refer to a time average. We do not measure dT/dx directly; rather, we infer it from the measured time derivative dT/dt via Taylor's frozen flow hypothesis

$$\frac{dT}{dx} = \frac{1}{u} \frac{dT}{dt}, \tag{3}$$

where u represents the flow speed past the thermistor. Following Osborn and Cox (1972), the eddy diffusivity is defined through the turbulent temperature variance equation, assuming isotropic turbulence acts on a background state with the only mean gradient in the vertical coordinate direction, dT/dz. From this, the eddy diffusivity for heat is

$$K_T = \frac{\frac{1}{2}\chi_T}{\langle dT/dz \rangle^2}. \tag{4}$$

The wavenumber extent of Ψ_{T_x} depends on ϵ through the Batchelor wavenumber $k_b = \left[\epsilon/\left(\nu D_T^2\right)\right]^{1/4}$. Because thermistors typically capture a small fraction of temperature gradient variance (Lueck et al. 1977; Nash et al. 1999), k_b must be estimated to determine χ_T from partially resolved spectra. In the absence of direct measurement of the microscale velocity shear, we make the assumption that $K_\rho = K_T$ to determine ϵ and hence k_b (i.e., Alford and Pinkel 2000). Here,

$$K_\rho = \Gamma \epsilon / N^2 \tag{5}$$

is defined assuming a steady-state balance between shear production, turbulence energy dissipation, and buoyancy production J_b, with a constant mixing efficiency Γ setting the ratio between ϵ and J_b (Osborn 1980). Assuming the equality of Eqs. (4) and (5),

$$\epsilon_\chi = \frac{N^2 \chi_T}{2\Gamma \langle dT/dz \rangle^2}, \tag{6}$$

where ϵ_χ denotes ϵ computed from χ_T.

b. Estimating χ_T

Because flow speeds are typically large (and variable) and computations are made over short time intervals (for reasons discussed in section 6), gradient spectra contain only a small fraction of the diffusive subrange at moderate dissipation rates, with the highest wavenumbers almost always attenuated because of sensor response. As a result, individual spectra seldom look like the canonical Batchelor (1959) form, so curve-fitting procedures (e.g., Luketina and Imberger 2000) fail to be robust. In contrast, the procedure we use is insensitive to the shape of the temperature gradient spectrum and in no way requires that the diffusive roll-off be resolved.

Our procedure does require Γ; however, the dependence on it is weak (see appendix).

To estimate χ_T when the spectrum is incompletely resolved requires fitting observed spectra over limited bandwidth to an accepted universal form. In practice, we determine χ_T by integrating $\Psi_{T_x}(k)$ over a subrange $k_{\min} < k < k_{\max}$ that is resolved by the thermistor. Because the frequency-response transfer functions we determine for each thermistor (see section 4) are neither perfect nor do they extend to k_b for high ϵ and u, we account for variance not resolved by the probe by assuming a universal form for the scalar spectrum at unresolved wavenumbers. The variance between the measured $[\Psi_{T_x}(k)]_{\text{obs}}$ and theoretical $[\Psi_{T_x}(k)]_{\text{theory}}$ spectra at resolved wavenumbers is assumed to be equal:

$$\int_{k_{\min}}^{k_{\max}} [\Psi_{T_x}(k)]_{\text{obs}} dk = \int_{k_{\min}}^{k_{\max}} [\Psi_{T_x}(k)]_{\text{theory}} dk. \qquad (7)$$

Then χ_T is computed from the full integral of the theoretical spectrum. Theoretical forms for the scalar spectra have been proposed by Batchelor (1959) and Kraichnan (1968). It has been found that Kraichnan's universal form more closely matches both field observations (Nash and Moum 2002) and fully resolved turbulence simulations (Smyth 1999). We use the Kraichnan form here but note that this choice has little quantitative effect on our results.

The wavenumber extent of the theoretical scalar gradient spectrum depends on the value of the universal constant q and the Batchelor wavenumber, which we estimate through Eq. (6) as $k_b = [\epsilon_\chi/(\nu D_T^2)]^{1/4}$. We use an iterative procedure to determine χ_T and ϵ_χ that is consistent with Eqs. (2), (6), and (7) for nominal values of Γ(0.2) and q(7), initial values of $k_{\min}$ and $k_{\max}$, and measured values of N^2, dT/dz, and Ψ_{T_x}. The procedure is as follows: First we estimate χ_T based on an initial guess of k_b. We set $k_{\max} = k_b/2$ or to a wavenumber equivalent to $f = 40$ Hz [i.e., $k_{\max} = 2\pi(40)/u$], whichever is smaller. We then use Eq. (6) to refine our estimate of k_b and recompute χ_T using Eqs. (2) and (7). This sequence is repeated and converges after two or three iterations. Estimates of χ_T from this iterative procedure are equivalent to the explicit formulation of Alford and Pinkel (2000), except that we use the Kraichnan form of the spectrum. Biases associated with this procedure are explored in the appendix.

c. Flow speed past the thermistor

Instruments on a mooring with a buoyant surface expression are subjected to pumping at surface wave periods. This means that the flow speed u past a sensor is the vector sum of the fluid speed U and the speed at which the instrument package (or the cable to which it is attached) moves because of surface-induced pumping. In the case that the sensor is aligned with the fluid flow in the x_c coordinate direction (as in Fig. 2), the flow speed past the sensor is

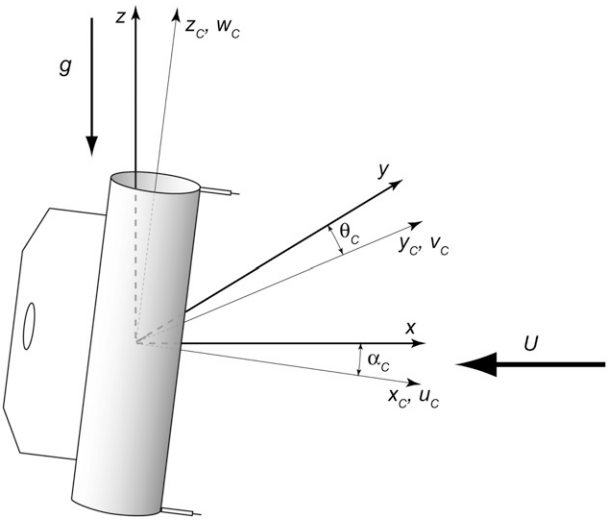

FIG. 2. Schematic showing the coordinate system in the χpod reference frame, denoted by x_c, y_c, z_c; U is the current speed; and g the gravitational acceleration. The earth's reference frame is denoted by x, y, z and is aligned with g; here α_c and θ_c represent angles of rotation about y and x axes, respectively (i.e., pitch and roll).

$$u = \sqrt{(U + u_c)^2 + v_c^2 + w_c^2}. \qquad (8)$$

The cable velocities u_c, v_c, and w_c can be deduced from measurements using motion sensors. Measured accelerations in orthogonal coordinates (x_c, y_c, and z_c, where $z_c > 0$ is upward) are

$$\begin{aligned} a_c^x &= -g \sin\alpha_c + \dot{u}_c, \\ a_c^y &= -g \sin\theta_c + \dot{v}_c, \quad \text{and} \\ a_c^z &= -g \cos\alpha_c \cos\theta_c + \dot{w}_c \simeq -g + \dot{w}_c, \end{aligned} \qquad (9)$$

where the overdot denotes the time derivative, and the approximation for the vertical component holds for small angles. The accelerations [Eq. (9)] include a gravitational component (tilting) and an inertial component. The tilts α_c and θ_c are typically referred to as pitch and roll. A full motion package, including linear accelerometers and angular rate sensors, would allow unambiguous distinction between tilting and inertial accelerations, as well as evaluation of angular velocities at the thermistor tip. Because of power and data storage constraints, our package included only orthogonally mounted linear accelerometers. Although our estimates

of w_c are unambiguous, there exists ambiguity in our estimate of u_c and therefore, uncertainty in u. The effect of this on our estimate of χ_T is addressed in section 6.

3. Design considerations

We anticipated three major problems in making a successful measurement of mixing from a mooring:

- ensuring that the sensors are exposed to undisturbed flow;
- contamination of the measurement by cable motion; and
- biological fouling of the sensors through either mechanical destruction by large creatures or biological growth, including the buildup of a bacterial film on the thermistor glass, which we imagined could slow the heat transfer between water and sensor, thereby reducing the sensor's frequency response.

Consideration of these issues helped dictate the final design of χpod—complicating the design but ultimately making the measurement successful. We discuss each problem in turn, our design solutions, and the overall construction of χpod.

a. Exposure of sensors to undisturbed flow

Measurements of small-scale microstructure fluctuations of temperature, conductivity, or velocity on profilers (Moum et al. 1995) or towed bodies (Moum et al. 2002) are possible in part because sensors are located at the leading edge of an instrument package that moves relative to the fluid, either by freely falling or by being towed through undisturbed fluid. On a mooring, sensors must be clamped to the mooring cable and mean currents relied upon to refresh the sampled fluid. To sense undisturbed fluid, they must either be made to swivel to the upstream side of the cable or multiple sensors must be deployed so that at least one is upstream of the cable. We chose to orient χpod using a vane diametrically opposed to the sensors (Figs. 1 and 2). This follows a design similar to that used on the TAO moorings to reduce contamination in Doppler current measurements (Freitag et al. 2003). Rather than use a separate mechanical swivel, measurements of the torsional rigidity of the cable (1.27-cm diameter jacketed steel Nilspin) indicated that a vane of width 15 cm and length 75 cm (similar to that shown) would provide enough hydrodynamic torque to the package at speeds greater than about 0.1 m s^{-1} even if adjacent units were clamped in opposition to each other at 1-m intervals (the worst-case scenario for deployment at sea). This was confirmed by numerous tests of multiple units on cabled moorings in Yaquina Bay, in which currents change direction on tidal periods and range from 0 to 1.5 m s^{-1}.

To monitor the relative directions of ambient currents and the χpod vane, a compass was installed. In the event that the vane did not provide sufficient steerage to expose sensors to the upstream side of the cable, data were flagged.

b. Cable motion

Microstructure measurements from profilers and towed bodies also require the instrument package to be sufficiently quiet (in a hydrodynamic sense) that package motions do not contaminate the measurement.[1] In preparation for the proposal that funded this development, we first sought high-frequency (0.1–100 Hz) accelerometer data from moorings that might provide us guidance on broadband cable motion. Finding none, we performed simulations in which we sampled a two-dimensional field of synthetically generated temperature microstructure that obeyed a Batchelor wavenumber form along the path induced by mooring motion at a range of frequencies and amplitudes of current speed–induced cable oscillations. These indicated that spectral contaminations would be acceptable if peak-to-peak cable oscillations in the data band remained below about two cable diameters.

c. Biological fouling

For use in other instrumentation, we typically manufacture our sensor stings (which house the thermistor beads) from stainless steel. For these long χpod deployments, the stings were constructed from copper, a known biological poison, as a means of discouraging growth on the thermistors. Upon recovery from our first 4-month deployment in fall 2005 there was growth on the acetal pressure case but none on the copper stings. Nor was there any indication of a reduction in the frequency response of the sensors.

For this first deployment, we decided to fully expose sensors, hoping that the cable clamps and cable would provide enough protection from mechanical breakage due to marine life or fishing line. As it turned out (section 5a), this was not sufficient to prevent breakage, so we have since added small probe protectors (shown in Fig. 1c); these have contributed to uninterrupted records over a subsequent 8-month deployment at four depths.

[1] These requirements are less stringent for temperature or conductivity than they are for velocity (Lueck et al. 2002).

TABLE 1. χpod sensors.

Signal	Sensor	Manufacturer/model	Temporal resolution	Signal resolution	Sample rate (Hz)
Pressure	Piezoresistor	Measurement Specialties 86 (0–100 psi)		0.1% FSO	10
Linear acceleration	Piezoresistor	IC Sensors 3052 (0–2g)	0–250 Hz	0.5% FSO	120
Compass direction	Magneto-inductive	Precision Navigation, Inc. V2Xe (now using Honeywell HMC6352)		<1°	1
Temperature	Thermistor	GE/Thermometrics FP07	Variable nominal 3 db, 20–30 Hz	<100 μK	10
dT/dt	Thermistor	GE/Thermometrics			120

4. Instrument configuration

Our final design included two FP07 thermistors separated by 0.9 m (for redundancy and, with both working, to obtain a local estimate of heat flux divergence). These were calibrated in our laboratory as a function of temperature. For typical oceanic values of ϵ, FP07 thermistors are not fast enough to completely resolve the temperature variance at moderate flow speeds (i.e., $u > 0.2$ m s^{-1}). The frequency response of microbead thermistors is unique to individual thermistors (Nash and Moum 1999). For each thermistor, a frequency transfer function was determined from measurements in Yaquina Bay while mounted on our turbulence profiler *Chameleon* beside a thermocouple with much faster response (Nash et al. 1999). This, as well as a frequency transfer function to correct for antialiasing filters, was applied to restore lost variance to temperature gradient spectra prior to integration to compute χ_T (section 2). Error and bias associated with the response corrections are discussed in the appendix.

The thermistors were mounted on both end caps of a 0.75-m-long, 0.1-m outside diameter pressure case constructed of acetal with wall thickness 0.0095 m. These were sampled at 10 Hz and their differentiated signals (dT/dt) at 120 Hz (Table 1). Three orthogonally oriented 0–2-g linear accelerometers were sampled at 120 Hz. A compass was sampled at 1 Hz.[2] A pressure sensor ported through the lower end cap was sampled at 10 Hz. Data were sampled as 24-bit words and the most significant bits stored as 16-bit words. The total data rate of 631 16-bit words s^{-1} required storage on an internal IDE hard disk drive.[3]

To enable long deployments, the current load for both analog and digital electronics was minimized. The final design draws 24 mA average current over a 24-h cycle. For a 6-month deployment, this requires 20 lithium D-cell batteries. The pressure case is primarily a battery pack.

5. Results from the first deployment

Three χpods were deployed by National Oceanic and Atmospheric Administration (NOAA) personnel aboard the R/V *Ka'imimoana* on the TAO mooring at 0°, 140°W on 22 September 2005 and recovered on 16 January 2006. The TAO mooring configuration is discussed on NOAA's TAO Project Web site (http://tao.noaa.gov/). For this deployment, we purposely positioned χpods at 29, 49, and 84 m to be close to TAO temperature sensors at 28, 48, and 80 m and TAO current meters (Sontek Argonauts) at 25, 45, and 80 m. The TAO temperature sensors were sampled at 10-min intervals. The current data were sampled at 1 Hz and averaged to 10 min before storage. A nearby subsurface ADCP mooring provided hourly averaged currents from 3-s samples.

In this section, we discuss the temperature measurements and survivability of the thermistors, as well as the basic engineering measurements used to understand the behavior of χpod.

a. Thermistor survivability

Measurements of temperature from the dual thermistors on each of three χpods are compared to nearby TAO Sea-Bird Electronics MicroCat recorder (SBE37) measurements on the mooring cable (Fig. 3). The upper thermistor at 49 m was destroyed upon deployment. The lower thermistor at 49 m shifted voltage rapidly after 3 weeks but steadied and continued to track fluctuations in the TAO temperature measurement. The upper thermistor at 84 m drifted slowly by 1 V after 2 weeks and remained there for the remainder of the deployment. The lower thermistor at 84 m lasted the entire deployment and was destroyed on recovery. The remaining thermistors were apparently mechanically broken while on the mooring; the signal was lost (open

[2] We have since switched from a Precision Navigation, Inc. model V2Xe compass to a more reliable and higher-resolution Honeywell HMC6352.

[3] We expect that continued expanded capacity of flash cards and reduction in our data sampling will enable storage on compact flash.

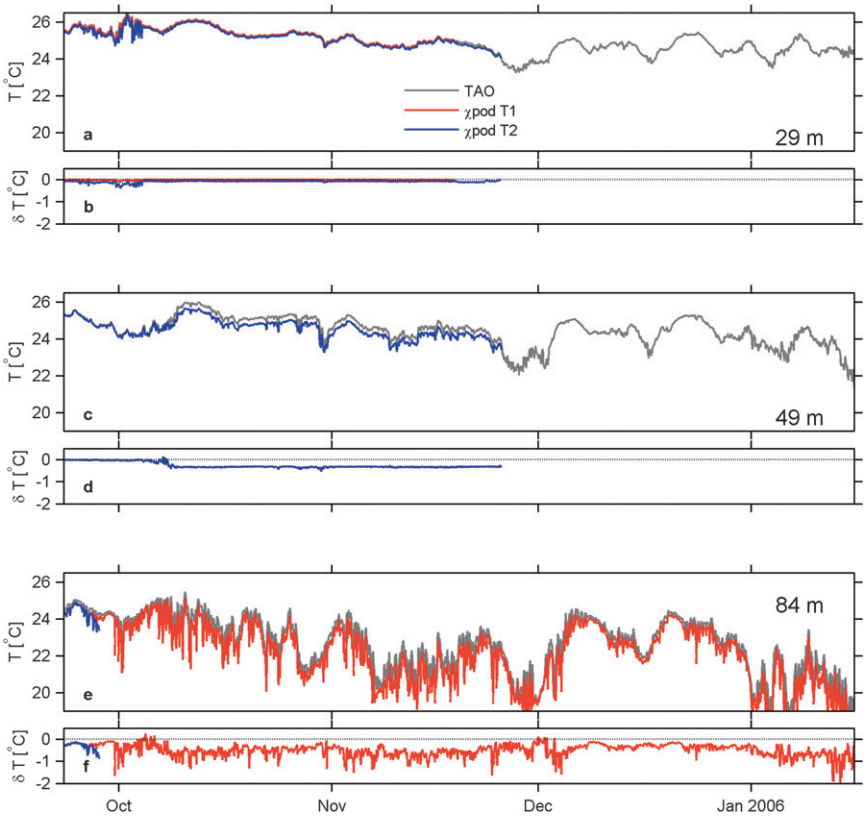

FIG. 3. (a),(c),(e) Temperature at 0°, 140°W September 2005–January 2006. Plotted in gray are temperature measurements at (a) 28, (c) 48, and (e) 80 m from SBE37 thermistors (10-min averages reaveraged to 75 min). Red traces are derived from the upper χpod thermistors, blue traces from the lower χpod thermistors at 29-, 49-, and 84-m depths. The data plotted are 75-min averages, which is the length of individual files written internally to χpod's disk drive. (b),(d),(f) Differences between χpod thermistor measurements and TAO temperature measurements ($\delta T = T_{\chi\text{pod}} - T_{\text{TAO}}$).

circuit voltage) between successive 10-Hz samples. The upper thermistor at 29 m broke in mid-November and the remaining two sensors (at 29 and 49 m) broke within 5 min of each other on 25 November. There was no evidence of fishing line entangled in any of the mooring gear recovered in January 2006. We suspect that schooling fish caused the breakage. Subsequent designs incorporate a protective copper housing to help prevent mechanical breakage of the tip (Fig. 2c). These have contributed to 80% data recovery in the August 2006–May 2007 deployment. With this configuration, and the dimensions noted in Fig. 2c, we do not expect there to be any contamination when the flow remains aligned within ±45° of head-on.

The temperature measurements shown were derived from our laboratory calibrations of thermistors. Aside from the drift at 49 m (Fig. 3c) that we cannot account for because the sensor was later broken, our calibrations agree to within 0.1°C of the TAO temperature measurements. The temperature difference ($\delta T = T_{\chi\text{pod}} - T_{\text{TAO}}$) and its variability can be attributed to the local temperature gradient and its temporal variations. Both the magnitude and variability in δT are largest at 84 m for two reasons. First, the separation between sensors is largest there: 4-m separation at 84 m compared to 1-m separation at 29 and 49 m. Second, both dT/dz and its variability is largest at 84 m. We note that δT is well described by $\delta z(dT/dz)$, where δz is the spacing between sensors and dT/dz is estimated locally from $T_{\chi\text{pod}}$ using the cable motion as described in section 5c.

b. *Steering and tilts*

Current speed and direction at 25-m depth are shown in gray in Figs. 4a,b. The direction of the vane is represented by the black trace in Fig. 4b. Unfortunately, our compass failed in mid-November. (In fact, all three

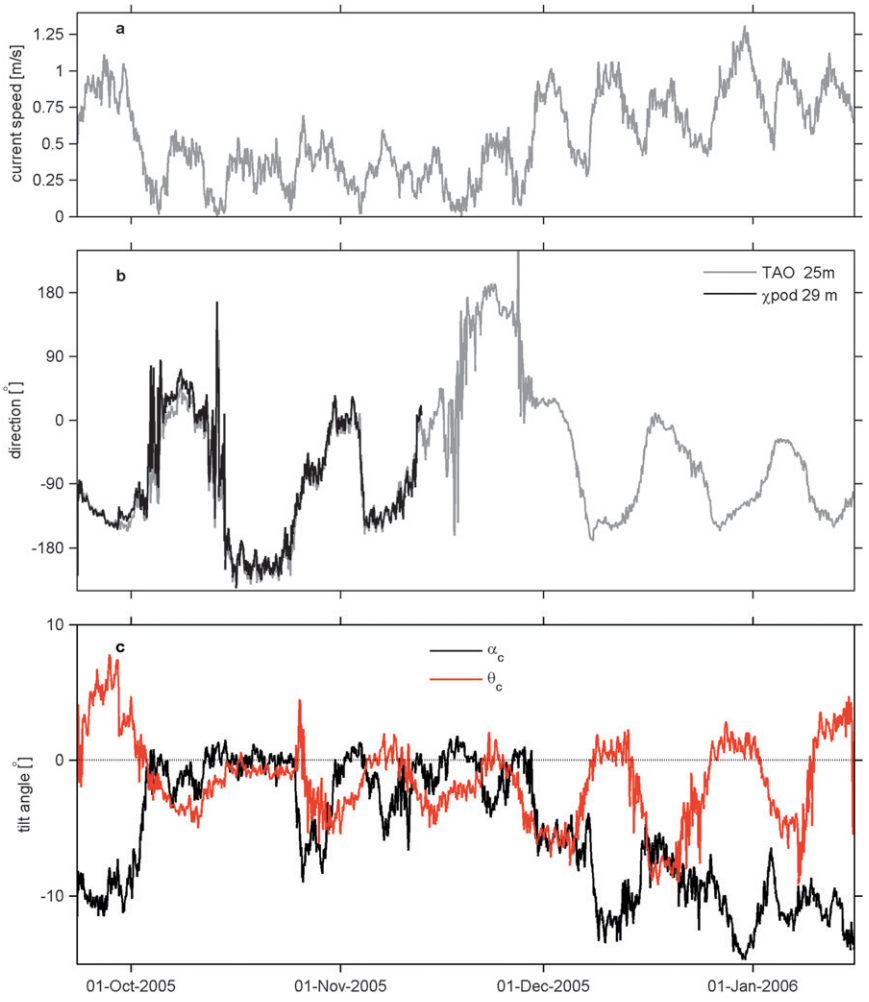

FIG. 4. (a) Current speed at 25-m depth as measured from a SonTek Argonaut on the TAO mooring. (b) Current direction from the measurement at 25-m depth (gray) and χpod direction at 29 m (black); χpod direction is defined relative to the vane and is 180° opposed to the temperature sensors. (c) χpod tilts as defined in Fig. 2.

compasses failed during the deployment; hence the switch to a new manufacturer.) Even at relatively slow current speeds (below 0.1 m s^{-1}) the vane was aligned with the currents to within 20°. At least on a mean basis, the package maintains a relatively constant heading, and the thermistors were steered into the flow to our satisfaction.

Mean body tilts were defined from the 75-min averages of linear accelerations, via Eq. (9), with the assumption that inertial accelerations do not contribute over long time scales. Tilts were speed dependent but limited to maxima of 13°. These were not entirely related to the current speeds at 25 m because there is strong veering of the currents in addition to direct atmospheric forcing on the surface float; both factors influence the shape of the cable.

c. *Cable motion*

The details of the motion of a point on the cable are considerably more complex than can be discerned from averaged data (Fig. 4). Without angular rate sensors, it is impossible to reconstruct the details of the motion because of the ambiguity in relative contributions of gravitational and inertial accelerations represented by Eq. (9); that is, we cannot tell the difference between tilting and cable accelerations. Because knowledge of the instantaneous speed of the fluid past the sensor is critical to our estimate of χ_T, both through Eq. (3) and in converting frequency to wavenumber for spectral comparison to a theoretical standard, we first consider the ranges of motions and later evaluate the consequences of uncertainties in it (section 6).

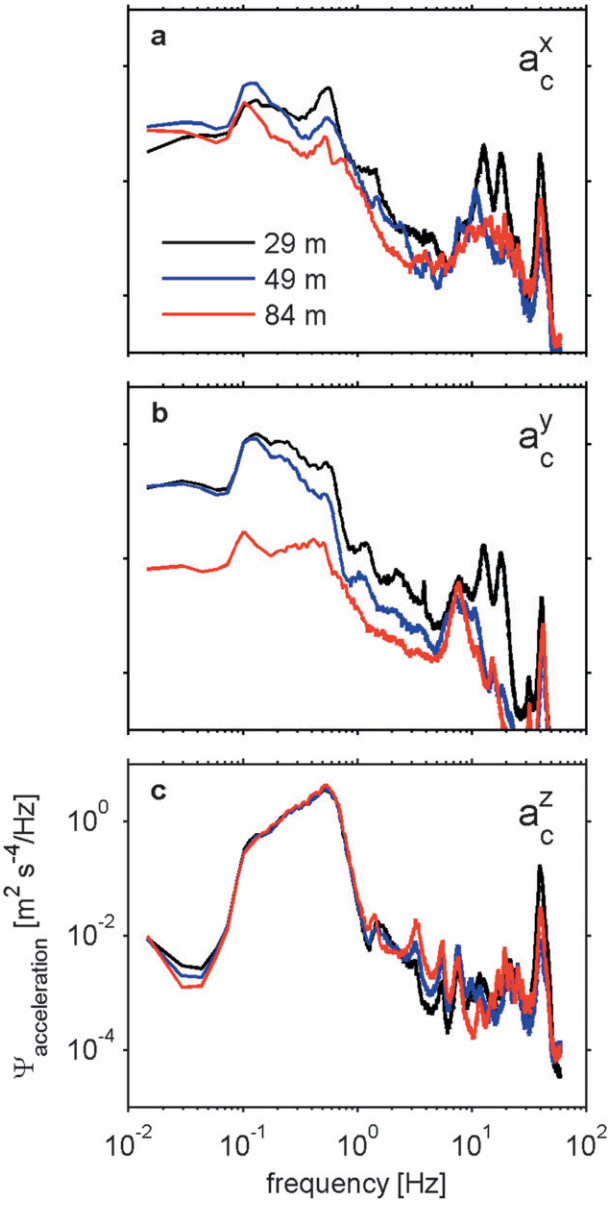

FIG. 5. Acceleration spectra in the three component directions: (a) x_c, (b) y_c, and (c) z_c. Colors correspond to the χpod units at 29 (black), 49 (blue) and 84 m (red). These spectra were computed from a 75-min record beginning at 2300 UTC 29 Sep 2005. Mean current speeds over this period were 1.0 (25 m), 0.6 (45 m), and 0.5 m s^{-1} (80 m).

Typical acceleration spectra (Fig. 5) show the influence of surface gravity waves (at 0.1–1 Hz) and of vortex-induced vibrations (at 5–20 Hz) in all components and at all χpod depths; the source of the 40-Hz signal is not clear. The effect of surface waves is largest in the vertical component (Fig. 5c), where it is equal in magnitude at all χpod depths. Wave signatures in the two horizontal components (Figs. 5a,b) differ although their magnitudes decay with increasing depth. Strouhal frequencies ($f_d = U/5d$) associated with the mean flow (U; noted in the caption) past the cable (diameter d) are 16 Hz at 25 m, 9 Hz at 45 m, and 8 Hz at 80 m. There is presumably broadband excitation associated with both the range of current speeds over the upper 100 m and the numerous other mooring components deployed along the cable. Cable displacements at high frequencies are found to be relatively small in the x_c and y_c directions; rms < 2 mm over 1–45 Hz and rms < 0.1 mm over 5–20 Hz.

For small tilts, the gravitational contribution to the vertical acceleration is negligible, so that the vertical speed is determined from $\dot{w}_c = a_c^z + g$ [Eq. (9)]. This is confirmed in Fig. 6a, which shows vertical cable velocity spectra coincident with spectra of the time derivative of depth (as sensed by χpod's pressure sensor) over the band of surface wave-induced motion; these two signals are coherent and in phase at all depths. Vertical excursions of ± 1 m and vertical speeds of ± 0.5 m s^{-1} at surface wave frequencies are common and of equal magnitude at all χpod depths. We conclude that the vertical cable speed w_c and displacement z_c are reliably determined from a_c^z.

Because there is significant vertical motion in the wind wave band that can be reliably estimated from our accelerometer measurements, we test how well these cable motions correspond to surface winds. Wind speeds measured from the surface buoy of the mooring were compared to rms values of w_c determined by integrating velocity spectra over $0.1 < f < 1$ Hz. This frequency band includes both wind waves and swell (Fig. 6a), although the vertical speed is dominated by frequencies in the wind wave range (Fig. 6b). Surface winds and rms vertical cable speeds are highly correlated (Fig. 7; rms values of w_c and mean values of U_{wind} were computed over 75-min periods for the entire 116-day record). This suggests that implementation of inexpensive and simple high-frequency motion packages on TAO moorings may be useful for determination of significant wave height.

One benefit of the large vertical excursions of χpod is that we can use these to derive a robust local estimate of dT/dz. We do this by fitting T to z over a time period that includes at least several wave periods (in the analysis to follow, we use 1 min).

THE SPECTRUM OF dT/dt

One adverse consequence of the cable motion is that the measured dT/dt can be dominated by vertical pumping of the sensor through a background vertical temperature gradient dT/dz when w_c is large (Fig. 8). In the swell data band (near 0.1 Hz), the example 5-h spectrum of dT/dt corresponds identically with that of

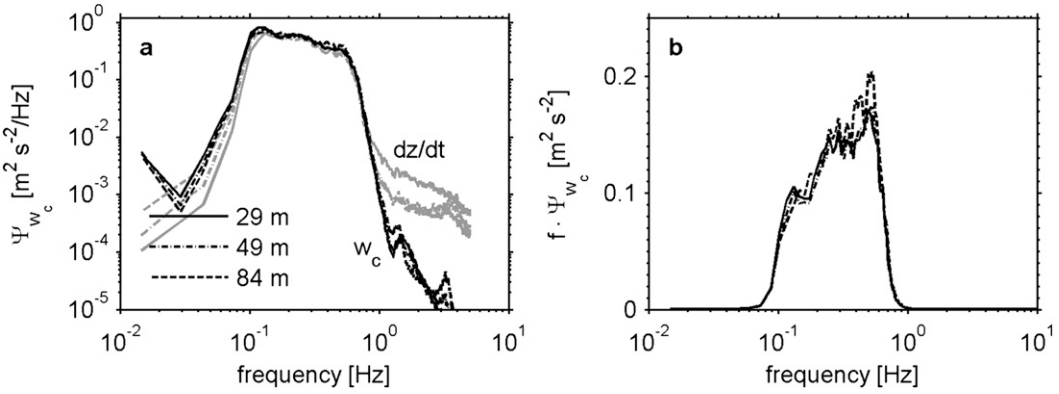

FIG. 6. (a) Spectra of the vertical component of cable velocity w_c (black) and of the time derivative of depth as measured by the pressure sensor dz/dt (gray) at the three depths; (b) w_c spectra in variance-preserving form.

$w_c dT/dz$ at both 49 and 84 m, where dT/dz is also large at this point in time. At 29 m, dT/dz is smaller, and surface wave contamination is barely apparent over the band $0.1 < f < 1$ Hz. Significantly, it is also evident from Fig. 8 that this band of contamination is distinct from the dissipation subrange used to compute χ_T (>2 Hz) and the internal gravity wave range $f < 0.1$ Hz. Note that these spectra only roughly resemble theoretical forms in the turbulence subrange because the tremendous range in both χ_T and ϵ over the 5-h period represented by Fig. 8 distorts the spectral shape.

d. Examples of high-frequency data

A short record of calibrated temperature and its fluctuations (Fig. 9) shows a few features. During this period, current speeds were 0.35–0.4 m s^{-1} at the χpod depth of 29 m. Presumably the dominant signal in Fig. 9 is the advection of fine structure and microstructure past the mooring by the mean flow. From analysis of TAO temperature sensors at 1, 5, 10, 13, 20, 25, and 28 m, the mixed layer deepened from about 5 m at 0200 UTC to about 25 m at 1000 UTC, part of the nighttime mixing cycle (the mixed layer depth is shown in another context in Fig. 15b). The sequence of sample records at increasing temporal resolution in Fig. 9 indicates the complexity of the temperature structure and how much of that complexity is not sampled at typical 10-min TAO temperature sample rates (gray dots in the figures). Although it cannot be seen on the scales shown in Fig. 9, the noise level of the temperature measurement is <1 mK. The precision of the measurement can be enhanced, if necessary, by incorporating the temperature gradient signal (Mudge and Lueck 1994).

6. Effects of cable motion

The flow speed past the sensor is given by Eq. (8). The vertical component of cable velocity is determined unambiguously from Eq. (9) and must be included in u. The horizontal components of velocity cannot be unambiguously determined from linear accelerations alone; that is, a_c^x can arise from inertial acceleration, tilt, or a combination of the two. However, we find v_c to be small compared to w_c so we ignore its contribution to u. We then use a_c^x to set bounds on u_c. If a_c^x is due solely to inertial acceleration, then

$$u = \sqrt{(U + u_c)^2 + w_c^2}, \tag{10}$$

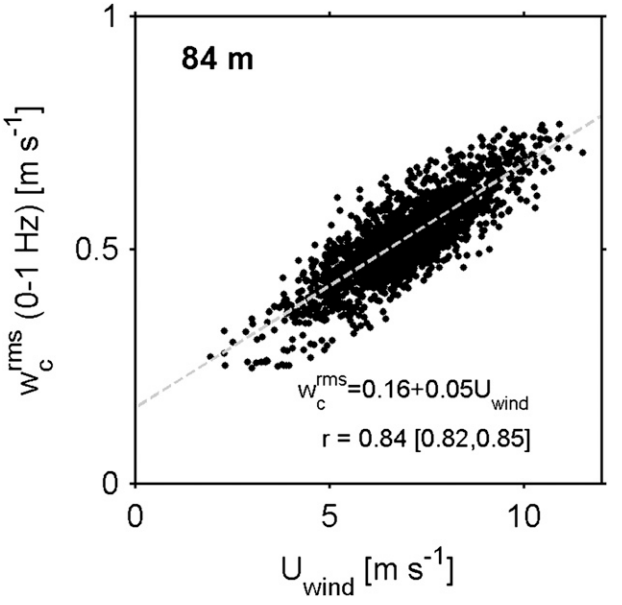

FIG. 7. Comparison of wind speed from the TAO surface meteorological package at 0°, 140°W and the vertical component of cable speed w_c at the lowest χpod, 84 m. Linear fits and correlation coefficients (95% confidence interval) are shown at lower right. These statistics are identical at all three χpod depths.

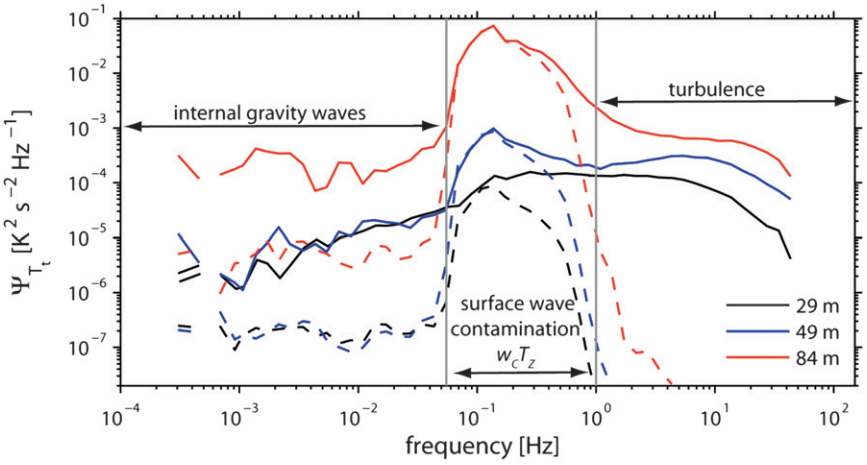

FIG. 8. Frequency bin-averaged spectra of dT/dt over a 5-h period at 29, 49, and 84 m (solid lines). The dashed lines represent spectra of $w_c dT/dz$. The frequency bands associated with internal gravity waves, surface gravity waves, and turbulence are noted.

where u_c is computed as $\int a_c^x dt$. Because there is undoubtedly some unknown contribution of tilt to a_c^x, we consider Eq. (10) a bound on u. At the other extreme, we suppose that our measurement of a_c^x is solely due to tilting, in which case

$$u = \sqrt{U^2 + w_c^2}. \tag{11}$$

Because u_c can add or subtract from U, its effect is to broaden the distribution of u estimates according to Eq. (10) relative to those deduced from Eq. (11). The bias is clearly seen in Fig. 10, as is the positive skewness resulting from the fact that U is always >0, whereas u_c is nearly equally <0 and >0. Consequences are addressed in this section.

Three complications arise because of the induced cable motions. First, vortex-induced vibrations cause flow speed variations with many cycles over a 1-s spectrum (Fig. 5). Second, surface wave–induced cable motion results in flow speed variations over a fraction of a cycle in a 1-s spectrum (Fig. 6). Finally, the ambiguity associated with Eq. (9) means that there is uncertainty in the correct value of u that applies to a given sample.

Flow speed variations due to cable motion cause the sensor to follow a contorted three-dimensional path through the turbulent flow field. This complicates our use of Eq. (3) (used to infer spatial gradients from temporal gradients) because u (the advecting flow speed past the sensor) is not constant over the 1-s period during which we compute a spectrum. It also leads to a distortion of the wavenumber inferred from the alternate form of Taylor's frozen-flow hypothesis, $k = f/u$.

We have addressed the first two complications using sensitivity studies on simulated turbulent flow fields in which we resampled temperature gradients along the contorted path and at the speed prescribed by either vortex-induced oscillations or by measured surface wave–induced flow speed variations.[4] In the first case, we determined that the spectral distortion resulting from cable oscillations larger than two cable diameters d was insufficient to cause more than a 20% bias in χ_T. Because we also calculated the maximum observed cable oscillations [from double integration of Eq. (9)] to be rms $< 0.15d$ over 1–45 Hz and rms $< 0.005d$ over 5–20 Hz, we conclude that this factor does not cause a serious bias in our estimate of χ_T.

Because wave-induced speed variations contaminate dT/dt between 0.1–1 Hz, we compute χ_T from windowed and detrended 1-s segments. The use of such a short record minimizes both the variability of u over individual spectra and the contributions from $w_c dT/dz$ to dT/dx. Although this period is shorter than we might have preferred, it is no different from what we typically choose when computing spectra over 1-m intervals from our turbulence profiler while profiling at 1 m s^{-1}.

Sensitivity studies on the consequences of flow speed variations from surface waves over a 1-s spectral estimate suggest that these can at worst introduce a 15% spread in the distribution of possible values of χ_T in a turbulence field characterized by a factor of 2 spread in χ_T due solely to natural intermittency. We conclude that flow speed variations caused by surface wave–induced cable motion (sub-1-s time scales) do not significantly affect our estimates of χ_T.

[4] We refrain from reporting the details of these computations here because we also find neither of these problems to be serious.

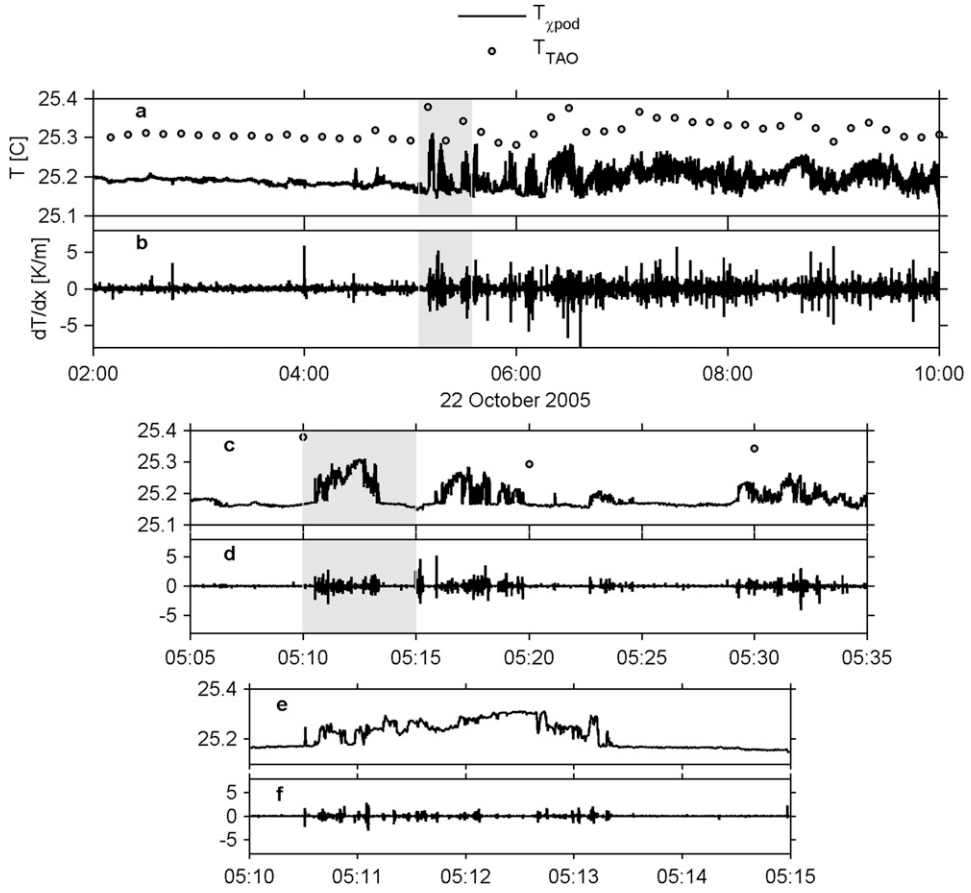

FIG. 9. (a) An 8-h record of temperature measurements at 28-m depth and 10-min intervals from the TAO SBE37 (gray dots) and at 29 m from χpod. The black trace represents temperature measured from the upper thermistor. (b) Temperature gradient dT/dx from χpod. The shaded region represents the period shown in the expanded plots labeled (c), (d); the shaded regions in (c), (d) are expanded in (e), (f).

The more significant problem is associated with our uncertainty in the correct value of u in a 1-s average. This is tested using the potential range of u suggested by our measurements of currents and χpod accelerations applied to computing χ_T from measurements of dT/dt. In the following we use a 48-h record from 28–29 September 2005 to estimate the effect of uncertainty in u on χ_T.

The uncertainty in u is represented by the differences in the two estimates computed through Eqs. (10) and (11) and is likely solely due to ambiguity in u_c. It seems that w_c is well defined (see Fig. 6) and that v_c is small relative to w_c. For these sampling tests, we suppose that Eq. (11) defines the true value of χ_T and that uncertainty is introduced by the addition of $u_c = \int a_c^x dt$, as in Eq. (10).

Examples of 1-s spectral estimates that have been corrected for the dynamic response of individual thermistors and for antialiasing filters are shown in relation to a Kraichnan spectrum in Figs. 11a–c. These were selected over a finite range of χ_T, ϵ, and u and then averaged in logarithmically spaced frequency bins. In each case, noise is apparent at high wavenumbers. At higher speeds (Figs. 11a,b), the spectra are flatter than the Kraichnan form, presumably because of frequency to wavenumber distortion when u changes appreciably over independent 1-s spectral estimates.

We suppose that the time scales for changes in χ_T are long relative to that for speed changes. That is, a stationary turbulence field is sampled many times at both low and high values of u, extrema of which occur at ~10-s intervals. We then compare distributions of χ_T obtained using all of the data (black line, Fig. 12) and compare these to distributions of χ_T obtained at high speeds ($u > 1.1$ m s^{-1}; red line) and at low speeds ($u < 0.9$ m s^{-1}; blue line). These indicate a clear but relatively small bias represented by the medians of 1-s χ_T estimates (the bias is $\simeq$25% low at high speeds and negligibly larger at low speeds).

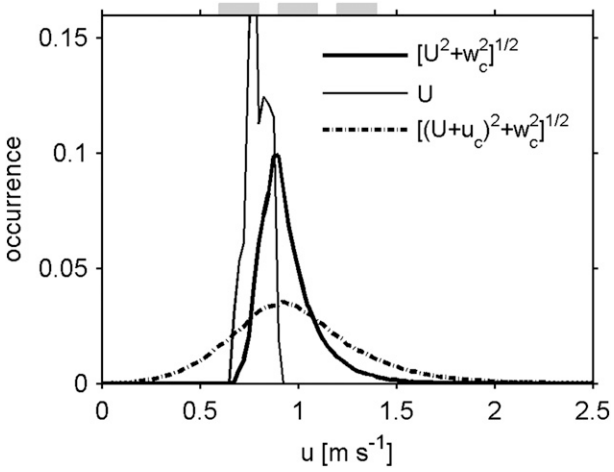

FIG. 10. Distributions of $u = \sqrt{U^2 + w_c^2}$ (thick solid line), U (thin solid line), and $\sqrt{(U + u_c)^2 + w_c^2}$ (dotted–dashed line) for the 48-h period of 28–29 Sep 2005 (also depicted in Figs. 11 and 12). The filled ranges at the top were used to select the data in Fig. 11.

We now use 1-s spectral estimates of χ_T from the same 48-h period to determine, on a point-to-point basis, the uncertainty in χ_T associated solely with our presumed uncertainty in u. The result (Fig. 13) indicates the uncertainty to be less than a factor of 3 95% of the time on 1-s estimates; it is roughly predicted by the curve $\left(U^2 + w_c^2\right)/[(U + u_c)^2 + w_c^2]$, which is how the estimate of χ_T is affected through Eq. (3).

Uncertainty is reduced considerably over a 60-s average (Fig. 14). This is due to the fact that the largest unresolved speed fluctuations (both positive and negative) are on periods significantly less than 60 s, so these are averaged. Presumably, the remaining (small) positive bias in χ_T results from the asymmetric curve in Fig. 13a. For further analysis of long time series, 60-s averages represent the base dataset.

It is very likely that short time scale variations cause local velocity fluctuations that are unresolved in the TAO velocity measurements. These may be due to phenomena such as narrow band internal gravity waves, for example, that are thought to play an important role in equatorial mixing (Moum et al. 1992b). It is unlikely, however, that the velocity signals of these are as large as the cable speeds induced by surface waves.

Other sources of uncertainty in our estimates of χ_T arise independently from uncertainties in the precise form of the theoretical spectrum, the magnitude of the mixing efficiency required to evaluate Eqs. (5) and (6), and the cutoff frequency determined to represent the dynamic response of individual thermistors. These are discussed separately in the appendix.

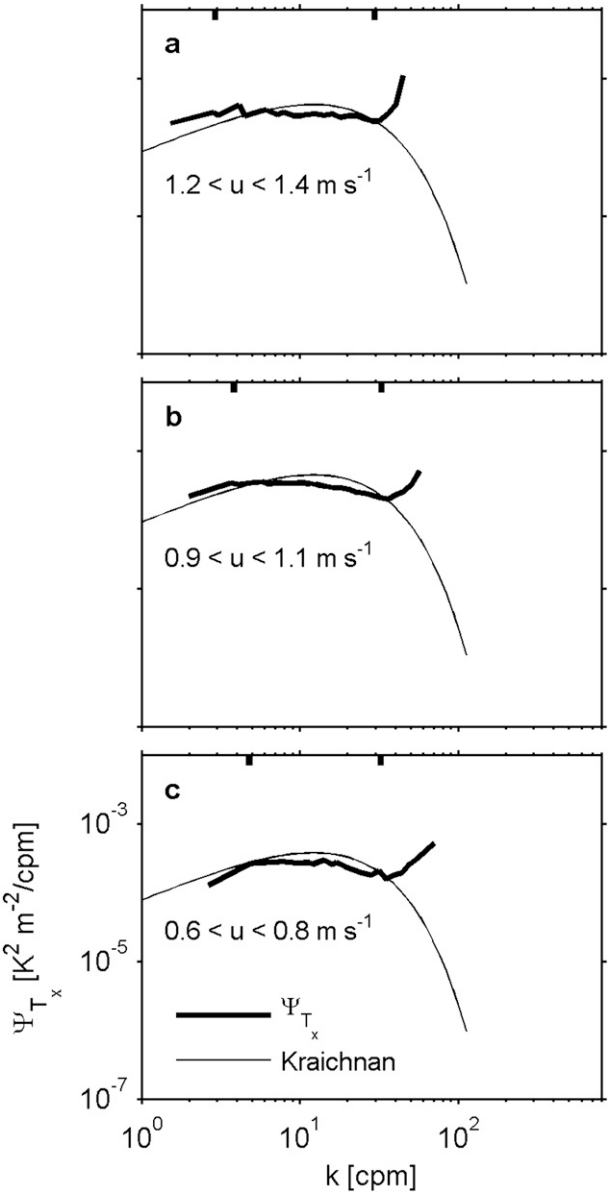

FIG. 11. Averaged 1-s spectra for the three filled ranges of flow speed u shown in Fig. 10: (a) 1.2–1.4, (b) 0.9–1.1, and (c) 0.6–0.8 m s^{-1}. Data were also selected with the following requirements: $8 \times 10^{-9} < \chi_T < 2 \times 10^{-8}$ K^2 s^{-1} and $7.5 \times 10^{-10} < \epsilon < 1 \times 10^{-9}$ m^2 s^{-3}. Integration limits for the computation of χ_T are denoted by the ticks on the upper axes.

7. Time series of χ_T, ϵ, and K_T and comparison to historical data

The purpose of this measurement is to obtain long, uninterrupted time series of equatorial mixing. In examining the entire record of this and following deployments, there appear to be many different mixing states; this is a focus of ongoing scientific analysis. For the purpose here of developing confidence in this new

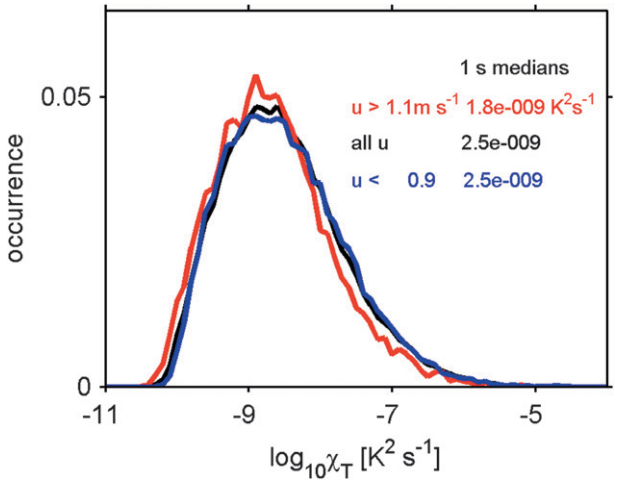

FIG. 12. Sample distributions of χ_T determined for all of the 1-s estimates over the 48-h period (solid black line) and for high speeds only (red line) or low speeds only (blue). Respective sample medians are indicated at upper right.

measurement, we consider a short, 4-day record (Fig. 15) that shows strong variability on a daily time scale. Here, the TAO buoy measurement of shortwave radiation distinguishes between night and day (Fig. 15a). Local temperature maxima ($\simeq$l0.1°C) at 29-m depth occur after sunset and are accompanied by high frequency-fluctuations (these are narrowband and near N; not shown here). The daily cycle is echoed in χ_T (Fig. 15e), ϵ (Fig. 15f), and K_T (Fig. 15g). In each case, day–night differences are about three to four orders of magnitude.

The daily cycle in turbulence has been previously documented at the equator (Moum and Caldwell 1985; Gregg et al. 1985; Moum et al. 1989) and associated with high-frequency (near-N), short wavelength (a few hundreds of m) internal gravity waves (Moum et al. 1992b). In particular, sample data from a 3 1/2-day time series in November 1991 (Moum et al. 1995) include intensive turbulence profiling with shear probes from which ϵ is directly estimated. *Chameleon* estimates of χ_T and ϵ are shown as red dots in Figs. 15e,f. The hours of day of the 1991 data are correct; the dates have been adjusted for comparision. Although these two sets of observations were made at the same location, they are separated in time by 14 yr and are derived from fundamentally different observations. Background currents and stratification also differ; how these differences affect mixing is an important scientific issue and a matter of a separate study that includes not only these measurements but also profiling measurements from 1984 and χpod measurements from 2006. Our purpose here is to identify a few similar characteristics. First, the ranges of

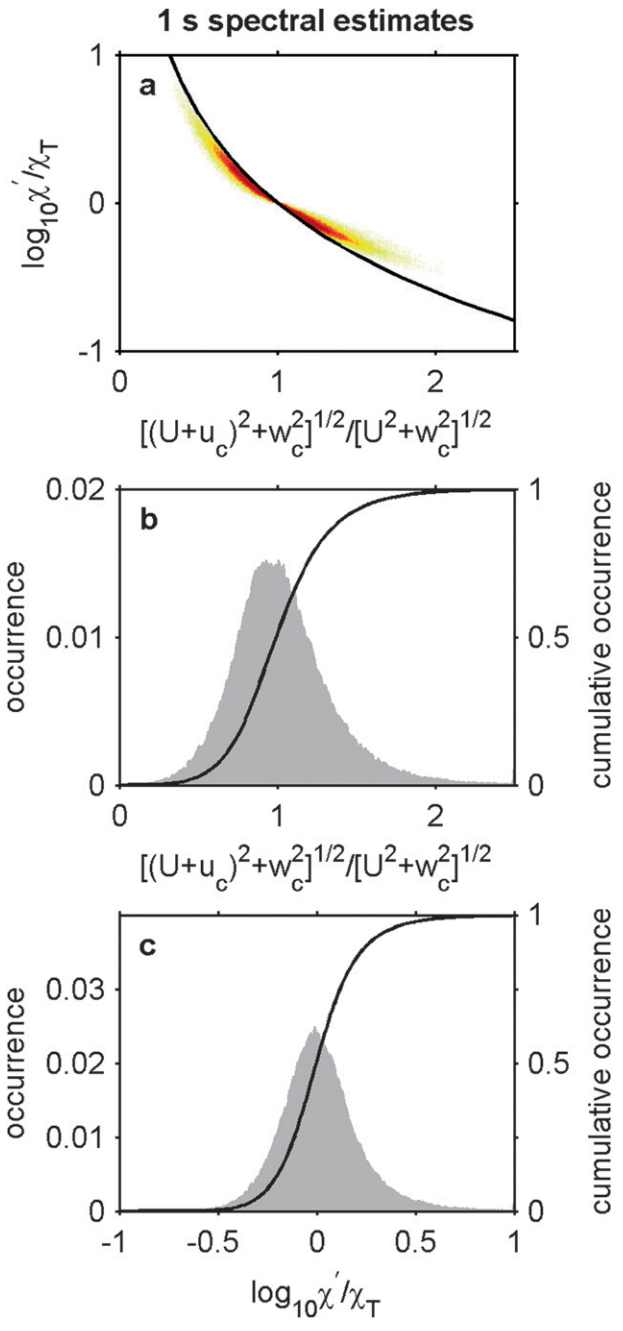

FIG. 13. Potential bias in 1-s estimates of χ_T due to our uncertainty in u. The data sample is 2 days (28 and 29 Sep 2005), which covers a broad range of speeds. The number of samples is 172 800. We assume here that the flow speed past the sensor is properly defined as $\sqrt{U^2 + w_c^2}$, from which we compute χ_T, and that the fluctuations due to u_c are spurious, resulting in the biased estimator χ'. (a) χ_T ratio vs speed ratio. The two-dimensional histogram of the data is represented by the image colors (red most frequently occurring). The solid line represents the curve $\left(U^2 + w_c^2\right) \Big/ \left[(U+u_c)^2 + w_c^2\right]$. (b) Distributions of speed ratios, including cumulative distribution (solid line) annotated on the right axis. (c) Distributions of χ_T ratios; $\chi'/\chi_T > 1$ indicates a low bias of our estimate χ_T. 95% limits on χ'/χ_T are [0.5, 3].

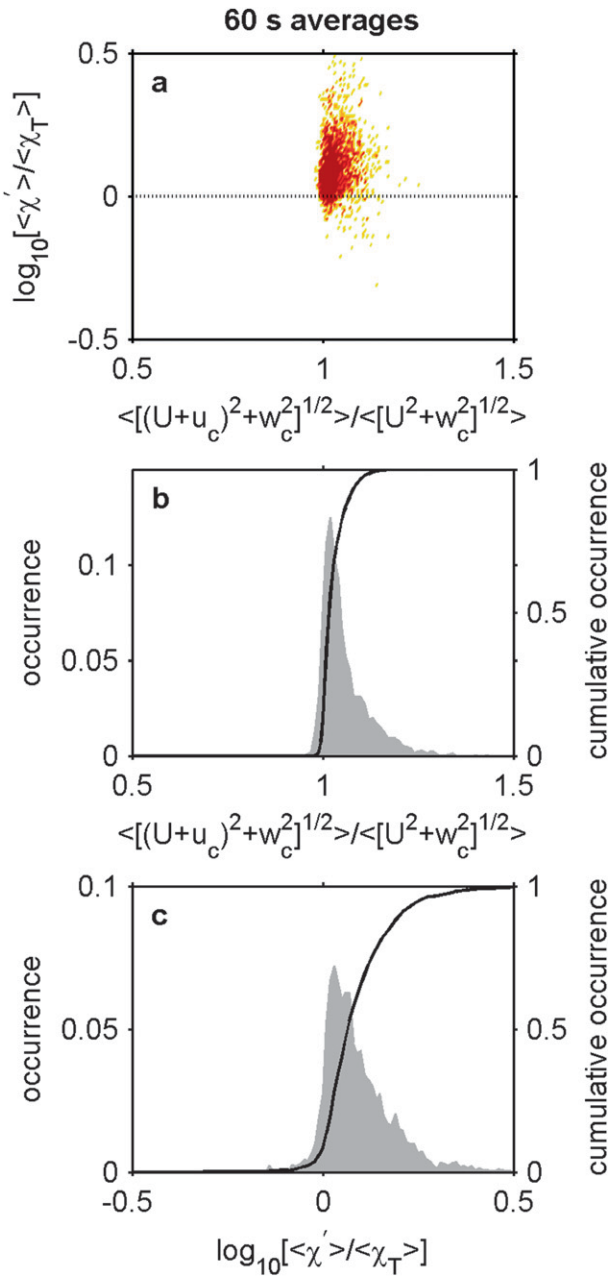

FIG. 14. As in Fig. 13, but the values are 60-s averages of the 1-s data. Note scale changes; 95% limits on χ'/χ_T are [0.9, 2].

magnitudes of χ_T and ϵ, although not identical, are not very different. This is more easily seen in Fig. 16, which shows perhaps a lower noise level in χ_T from the 1991 profiler measurements and a tendency to larger values of ϵ, which may be due to differing oceanographic forcing of turbulence between the two measurement periods. Second, the daytime suppression of χ_T and ϵ is in phase between the two datasets, although both the timing and magnitude of nighttime excitation differ. And finally, the total day/night variability is nearly the same (three to four orders of magnitude in both χ_T and ϵ).

As a final sampling test on the uncertainty in χ_T caused by uncertainty in u, we reconsider the χpod data represented by Figs. 15 and 16. The entire 4-day record was recomputed using both Eqs. (10) and (11) and the results were summarized in Fig. 17. The result is that 95% of the values of 60-s estimates of χ_T are within a factor of 2 of each other.

8. Summary and conclusions

At the design stage, we had full confidence that we could reduce power consumption and increase data storage sufficiently to execute long and continuous deployments that included not only the basic measurement of temperature and its high wavenumber gradients but also a measure of the instrument package motion. We were more concerned that bare thermistors would not survive long deployments, that they would not be reliably exposed to undisturbed flow, or that vortex-induced vibrations might contaminate the measurement. Fortunately, none of these factors have been limiting. Although mechanical breakage of sensors on the first deployment led to shortened records, our subsequent addition of protective rings to the sensors has resulted in much higher data recoveries.

The use of a vane to steer the χpods has been a successful means of keeping the sensors exposed to undisturbed fluid, at least at the range of current speeds observed to date. Although vortex-induced vibrations of the moored cable are clearly evident (Fig. 5), their amplitudes are sufficiently small (no more than 0.15 cable diameters rms across all potentially excited frequencies) that their effect on the measurement of χ_T is imperceptible.

A potentially more critical problem has been the large surface wave–induced cable motions that cause vertical displacements of ± 1 m and vertical cable speeds of ± 0.5 m s^{-1} in the surface wave frequency band (2–10 s). One of two unanticipated benefits has been that χpod acts as a vertical profiler (at least over limited range), yielding a robust local measure of dT/dz. Also, because the spectral energy of w_c is dominated by frequencies in the wind wave band (Fig. 6), there exists a close correlation to the surface wind speed (Fig. 7).

The vertical motion appears in the temperature gradient spectrum Ψ_{T_x} as $w_c\, dT/dz$, which clearly defines the band of frequencies contaminated by surface wave pumping (Fig. 8). At lower frequencies, we expect internal gravity waves to dominate. At higher frequencies, the turbulence subrange is apparently unaffected, thus

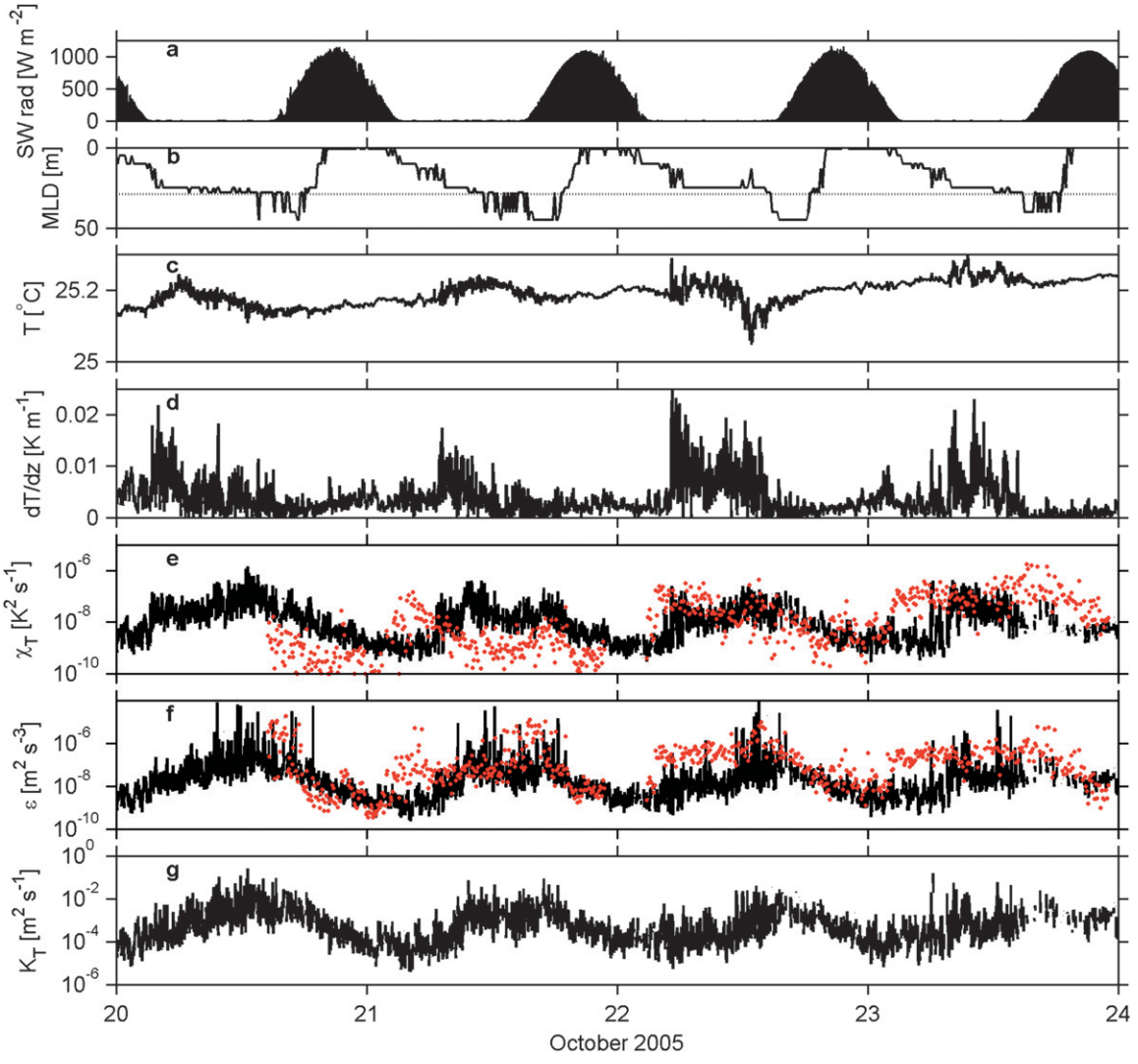

FIG. 15. A 4-day time series at 29-m depth. (a) Short-wave radiation from the TAO Atlas buoy. (b) Estimate of mixed layer depth (MLD) determined as the depth at which the TAO temperatures (nominal depths 1, 5, 10, 13, 20, 25, 28, 40, 45, and 48 m) deviate by 0.1°C from the value at the sea surface (1 m). The following data have been averaged to 60 s. (c) Temperature; (d) dT/dz, computed from a linear fit of T to z over a 300-s window about the 60-s average; (e) χ; (f) ϵ_χ; (g) K_T. Also plotted in (e) and (f) are the time series of χ_T, ϵ averaged over the depth range 26–33 m measured from *Chameleon* during the TIWE experiment in 1991 (red dots). Each dot is derived from a single profile. The TIWE data were obtained between 22 and 26 November 1991.

permitting our estimation of χ_T. In fact, Ψ_{T_x} (Fig. 8) looks very much like isopycnal slope spectra measured from the towed body *Marlin* (Klymak and Moum 2007), with the exception of the surface wave contamination in the moored spectra. Inasmuch as fluid is advected by the fixed sensors by the currents, the reference frame is similar and we might consider the moored measurements in the same framework, with the important caveat that the finite vertical extent of features propagating or advected through the highly sheared equatorial flow will complicate the interpretation in wavenumber/frequency space at a fixed point.

Because the cable speeds are of the same order as (and frequently much larger than) the advecting current speed, they represent a significant component of the flow speed past the thermistors. This motion must be included in our computations of χ_T through our use of Taylor's frozen flow hypothesis, both via Eq. (3) and in the frequency to wavenumber conversion $k = f/u$. Because the dominant motion is in the surface wave band (2–10 s), and we apply a constant value of u to evaluate both of these for spectral fitting [Eq. (7)], we minimize the change in u over a spectral estimate by choosing 1 s as the basis for estimating χ_T. However, the relative

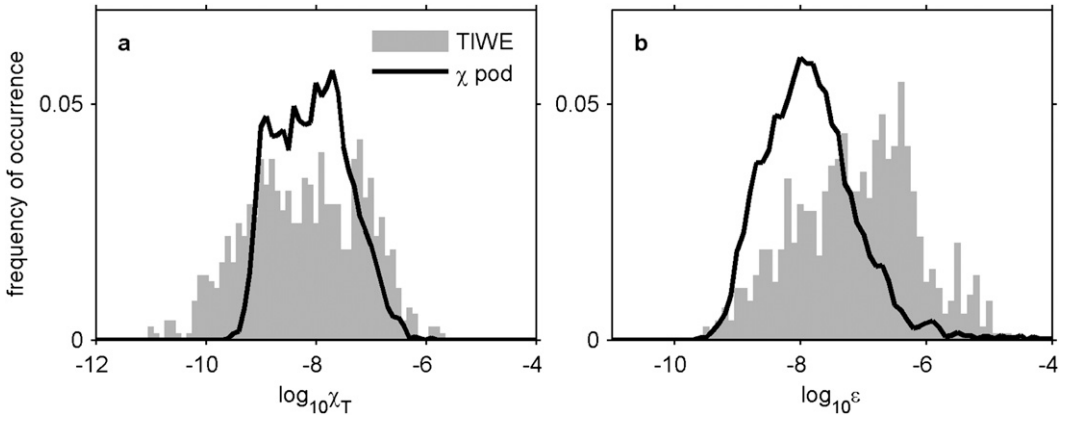

FIG. 16. Comparative histograms from the data shown in Figs. 15c,d: (a) χ_T; (b) ϵ. Gray area represents the TIWE data over 26–33-m depth range. The black line represents 60-s averages at 29 m. The TIWE χ_T estimates are derived from thermistor measurements on *Chameleon*, and the ϵ estimates from shear probe measurements; note the characteristic noise peak in the distribution of *Chameleon* shear probe estimates of ϵ at $\simeq 3 \times 10^{-10}$ m^2 s^{-3}, a peak not echoed in the inferred χpod estimate. The χpod data represent 4 days of 60-s averages of 1-s spectral estimates of χ_T as described in the text. The TIWE estimates were made from 728 individual *Chameleon* profiles through the 29-m depth range at 6–10-min intervals.

contributions of gravitational and inertial accelerations to measured horizontal components of acceleration is unknown [Eq. (9)], and hence our estimate of flow speed past the sensor has some uncertainty.

To reconcile our estimates of χ_T with this uncertainty in u, we conducted sampling experiments using both simulated spatial series of temperature gradients in a turbulent field as well as resampled χpod measurements with known bounds on u. The result is that although the uncertainty of individual 1-s estimates of χ_T is less than a factor of 3, 95% of the time, averaging nonetheless helps. On 60-s averages (about 10 cycles of the dominant contaminant motion), the uncertainty is less than a factor of 2, 95% of the time.

Although it has turned out that the expected bias to our estimate of χ_T is acceptably small, we have implemented angular rate sensors on a subset of χpods to be deployed at the equator in spring 2008. The measurements from these rate sensors, together with those from linear accelerometers, will provide an unambiguous description of the high-frequency motions experienced by the χpods.

Despite the adverse conditions under which these measurements were made, there are good reasons to have confidence in the estimates of χ_T, ϵ_χ, and K_T derived from them. Probably the biggest factor is quantitative comparison with historical data (Figs. 15 and 16). These indicate (from a selected sample) that

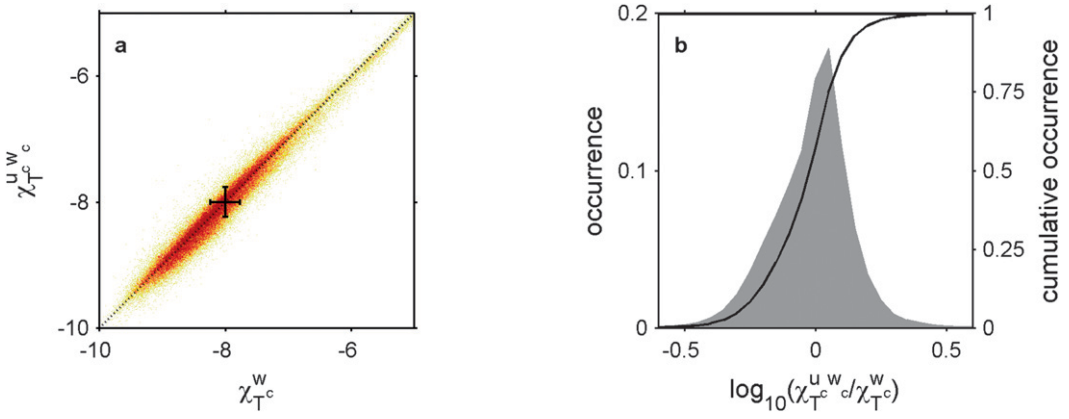

FIG. 17. (a) Comparison of χ_T estimates using u computed as Eq. (10) (ordinate) and as Eq. (11) (abscissa). The data represented by the abscissa are the 60-s averages displayed as time series in Fig. 15d. The lengths of the crosshairs are a factor of 3 in each direction. b) Histogram of the ratio of the two χ_T estimates (left axis), and cumulative occurrence (right axis); 95% limits on the ratio are [0.50, 1.7].

magnitudes of χ_T and ϵ and their variability, as well as their relative phase over several daily cycles, are not tremendously different from what was observed at a similar time of year in 1991.

The initial deployment discussed here has been followed by three others at the same site and at least one more is planned. Upon recovery of the first deployment of three χpods in January 2006, four χpods were deployed (29, 49, 59, and 84 m). The surface buoy broke free in May 2006 and has not been recovered. Those χpods are either still dangling beneath the buoy or on the seafloor. Five χpods were deployed in September 2006 (29, 39, 49, 59, and 84 m) and recovered in May 2007. This resulted in continuous records over the entire 8-month deployment at the upper four depths; the χpod at 84-m depth was damaged prior to deployment and recorded no data. Upon recovery an additional six χpods were deployed at 29, 39, 49, 59, 69, and 84 m. Ten χpods will be deployed on the TAO mooring at 0°, 140°W in spring 2008 and an additional ten on an ancillary adjacent mooring (R-C. Lien and M. Gregg, University of Washington) in fall 2008. During this latter deployment, we will execute an 18-day profiling station using *Chameleon*, acoustic Doppler current measurements, and high-frequency acoustic flow imaging echo sounder.

In addition, χpods have been deployed on a coastal mooring off Oregon (M. Levine, Oregon State University) and on drifters in the South China Sea (L. Centurioni and P. Niiler, Scripps Institution of Oceanography) and have been flown on gliders across both western and eastern continental shelves (K. Shearmann, Oregon State University; S. Glenn, Rutgers University). These have all been successful and have contributed additional and valuable learning experiences to our group as we continue to improve the basic χpod design.

Acknowledgments. This work was funded by the National Science Foundation (0424133). Ray Kreth and Mike Neeley-Brown (with help from Mark Borgerson, Oceanographic Embedded Designs) constructed the χpods. Alexander Perlin helped in organizing data. Numerous NOAA personnel have aided this effort with their professional handling of our instruments on deployment and recovery. The TAO mooring group at PMEL in Seattle were most helpful in sharing their expertise at the design and testing stage, in particular Paul Freitag, Andy Shepherd, and Chris Meinig. We are especially grateful to Mike McPhaden for his encouragement and support of this effort, and the TAO Project Office for continued support. Comments by Alexander Perlin, Emily Shroyer, and Yanwei Zhang on an early draft are appreciated. Insightful and constructive comments by three anonymous reviewers helped to sharpen several aspects of this paper.

APPENDIX

Uncertainties in χ_T due to q, Γ, and f_c

Our method of computing χ_T involves extrapolation of partially resolved spectra using a theoretical form to compute the total variance of dT/dx [Eq. (7)]. This procedure depends on three key parameters:

- q, the "universal" constant in the Kraichnan form of the theoretical spectrum;
- Γ, the mixing efficiency; and
- f_c, the cutoff frequency for thermistor corrections.

We have assumed each of these to be constant. While our choices are not arbitrary, to a certain extent their values are loosely constrained. Our objective here is to assess their contribution to the uncertainty in χ_T due to reasonable bounds on each. In addition, the uncertainty will depend on ϵ and u because these control the amount of variance resolved by a thermistor (i.e., the fraction of variance resolved increases for both low ϵ and low u). In the following, independent 1-s estimates of χ_T were computed while systematically varying q, Γ, and f_c to determine the relative effect of potential uncertainties in each on our estimate of χ_T (Fig. A1). We assume $q = 7$ and $\Gamma = 0.2$ as a baseline to compute χ_T, (these values are used for all of the computations made in this paper); χ' represents that computed with perturbed q, Γ, and f_c.

For fixed k_b, the wavenumber extent of Ψ_{T_x} depends on q. As a result, increasing q reduces the total variance for a given spectral level in the viscous-convective subrange. Hence, an overestimation in q will cause a reduction in χ'. Following Smyth (1999), $5 > q > 10$ represents an extreme range (for the Kraichnan form), with $q = 7$ being a likely value.

Note that Γ is required to estimate ϵ_χ through Eq. (6), so that k_b scales with $\Gamma^{-1/4}$. Although it is typically assumed that $\Gamma = 0.2$ (as we have done here), $0.1 > \Gamma > 0.35$ represents possible oceanographic bounds (Moum 1996; Smyth et al. 2001).

Finally, we allowed for uncertainty in the thermistor cutoff frequency f_c, which enters into Ψ_{T_x} through the single pole transfer function used for spectral corrections:

$$H^2(f) = \frac{1}{\left[1+(f/f_c)^2\right]}, \qquad \text{(A1)}$$

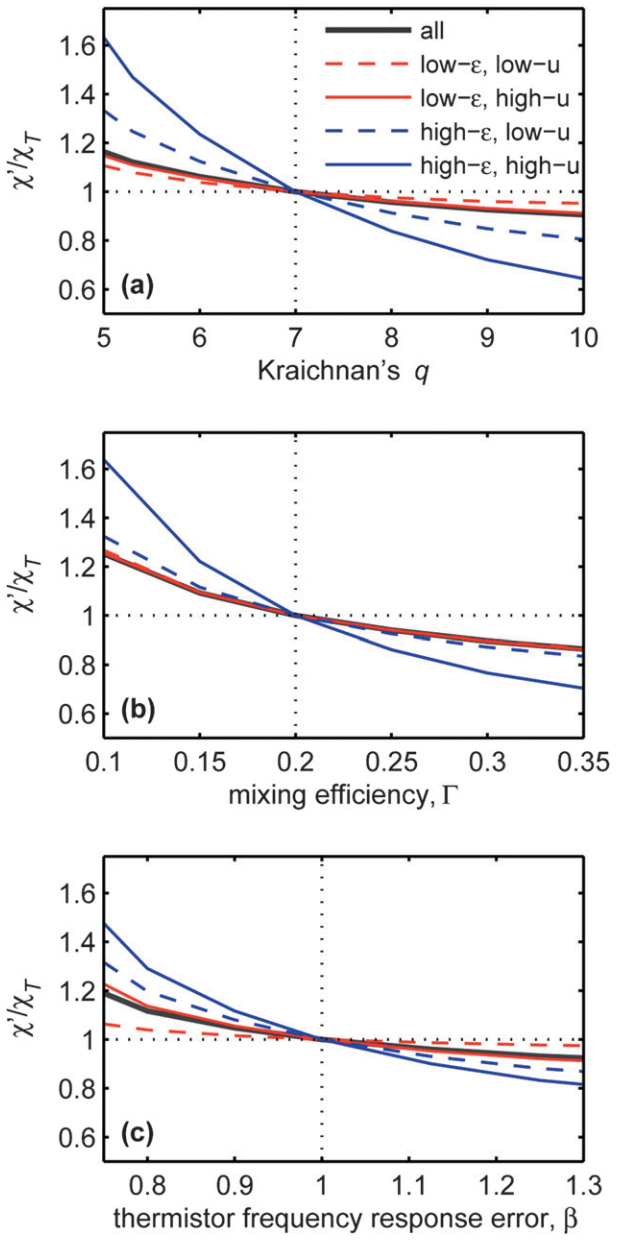

FIG. A1. Summary of sensitivity results. For each plot, 2×10^5, 1-s estimates of χ' were computed using altered values for (a) q, (b) Γ, and (c) β. In each plot, the mean bias in χ'/χ_T is plotted for various ranges of ϵ and flow speed u. High ϵ is $>10^{-7}$ m^2 s^{-3}, low ϵ is $<10^{-9}$ m^2 s^{-3}; high u is >1.0 m s^{-1} and low u is <0.7 m s^{-1}. Data from 20 and 28 October were used because these provide a broad range in u.

where $f_c \approx 20$ Hz is typical for our thermistors. Although we measure f_c prior to deployment (and use a different f_c for each thermistor), biological buildup could alter sensor response time. Our sensitivity test consisted of varying f_c according to $f_c^{\text{test}} = \beta f_c$ for β spanning from 0.75 to 1.3. For $\beta < 1$, too much response correction is applied, leading to increased χ'.

We also examined the effect of estimating dT/dz using different time intervals for averaging but found no associated bias.

The sensitivities, summarized as mean values of χ'/χ_T, are shown in Fig. A1. These are consistent with the above expectations. In all cases, biases increase with increasing ϵ and increasing u because these require the most spectral corrections. Only for the highest ϵ and u does the bias approach 1.5 for the most extreme values of q, Γ, and β. We thus conclude that biases associated with spectral extrapolation using improper parameters have a smaller effect on estimates of χ_T than potential bias caused by uncertainty in u (section 6).

REFERENCES

Alford, M. H., and R. Pinkel, 2000: Patterns of turbulent and double-diffusive phenomena: Observations from a rapid-profiling microconductivity probe. *J. Phys. Oceanogr.,* **30,** 833–854.

Batchelor, G. K., 1959: Small-scale variation of convected quantities like temperature in turbulent fluid. Part 1: General discussion and the case of small conductivity. *J. Fluid Mech.,* **5,** 113–133.

Freitag, H., M. McPhaden, C. Meinig, and P. Plimpton, 2003: Mooring motion bias of point Doppler current meter measurements. *Proc. IEEE Seventh Working Conf. on Current Measurement Technology,* San Diego, CA, IEEE, 155–160.

Gregg, M. C., H. Peters, J. C. Wesson, N. S. Oakey, and T. J. Shay, 1985: Intensive measurements of turbulence and shear in the Equatorial Undercurrent. *Science,* **318,** 140–144.

Klymak, J. M., and J. N. Moum, 2007: Oceanic isopycnal slope spectra. Part I: Internal waves. *J. Phys. Oceanogr.,* **37,** 1215–1231.

Kraichnan, R., 1968: Small-scale structure of a scalar field convected by turbulence. *Phys. Fluids,* **11,** 945–953.

Lien, R., D. R. Caldwell, M. C. Gregg, and J. N. Moum, 1995: Turbulence variability in the central Pacific at the beginning of the 1991–93 El Niño. *J. Geophys. Res.,* **100,** 6881–6898.

Lueck, R. G., O. Hertzman, and T. R. Osborn, 1977: The spectral response of thermistors. *Deep-Sea Res.,* **24,** 951–970.

——, F. Wolk, and H. Yamazaki, 2002: Oceanic velocity microstructure measurements in the 20th century. *J. Phys. Oceanogr.,* **58,** 153–174.

Luketina, D. A., and J. Imberger, 2000: Determining turbulent kinetic energy dissipation from Batchelor curve fitting. *J. Atmos. Oceanic Technol.,* **18,** 100–113.

McPhaden, M. J., 1993: TOGA–TAO and the 1991–93 El Niño–Southern Oscillation event. *J. Phys. Oceanogr.,* **6,** 36–44.

——, 1999: Genesis and evolution of the 1997–98 El Niño. *Science,* **283,** 950–954.

Moum, J. N., 1996: Efficiency of mixing in the main thermocline. *J. Geophys. Res.,* **101,** 12057–12069.

——, and D. R. Caldwell, 1985: Local influences on shear flow turbulence in the equatorial ocean. *Science,* **230,** 315–316.

——, ——, and C. A. Paulson, 1989: Mixing in the equatorial surface layer and thermocline. *J. Geophys. Res.,* **94,** 2005–2021.

——, D. Hebert, C. A. Paulson, and D. R. Caldwell, 1992a: Turbulence and internal waves at the equator. Part I: Statistics from towed thermistors and a microstructure profiler. *J. Phys. Oceanogr.,* **22,** 1330–1345.

——, M. J. McPhaden, D. Hebert, H. Peters, C. A. Paulson, and D. R. Caldwell, 1992b: Internal waves, dynamic instabilities, and turbulence in the equatorial thermocline: An introduction to three papers in this issue. *J. Phys. Oceanogr.,* **22,** 1357–1359.

——, M. C. Gregg, R. C. Lien, and M. E. Carr, 1995: Comparison of turbulence kinetic energy dissipation rate estimates from two ocean microstructure profilers. *J. Atmos. Oceanic Technol.,* **12,** 346–366.

——, D. R. Caldwell, J. D. Nash, and G. Gunderson, 2002: Observations of boundary mixing over the continental slope. *J. Phys. Oceanogr.,* **32,** 2113–2130.

Mudge, T. D., and R. G. Lueck, 1994: Digital signal processing to enhance oceanographic observations. *J. Atmos. Oceanic Technol.,* **11,** 825–836.

Nash, J. D., and J. N. Moum, 1999: Estimating salinity variance dissipation rate from conductivity microstructure measurements. *J. Atmos. Oceanic Technol.,* **16,** 263–274.

——, and ——, 2002: Microstructure estimates of turbulent salinity flux and the dissipation spectrum of salinity. *J. Phys. Oceanogr.,* **32,** 2312–2333.

——, D. R. Caldwell, M. J. Zelman, and J. N. Moum, 1999: A thermocouple probe for high-speed temperature measurement in the ocean. *J. Atmos. Oceanic Technol.,* **16,** 1474–1482.

Osborn, T. R., 1980: Estimates of the local rate of vertical diffusion from dissipation measurements. *J. Phys. Oceanogr.,* **10,** 83–89.

——, and C. S. Cox, 1972: Oceanic fine structure. *Geophys. Astrophys. Fluid Dyn.,* **3,** 321–345.

Smyth, W. D., 1999: Dissipation–range geometry and scalar spectra in sheared stratified turbulence. *J. Fluid Mech.,* **401,** 209–242.

——, J. N. Moum, and D. R. Caldwell, 2001: The efficiency of mixing in turbulent patches: Inferences from direct simulations and microstructure observations. *J. Phys. Oceanogr.,* **31,** 1969–1992.

Wang, W., and M. McPhaden, 2001: Surface layer temperature balance in the equatorial Pacific during the 1997–98 El Niño and the 1998–99 La Niña. *J. Climate,* **14,** 3393–3407.